ACS APPLIED NANO MATERIALS

www.acsanm.org Article

Surface-Facet-Dependent Electrochromic Properties of WO_3 Nanorod Thin Films: Implications for Smart Windows

R. Colby Evans, Rachelle Austin, Rebecca C. Miller, Alexander Preston, Zach N. Nilsson, Kaka Ma, and Justin B. Sambur*

Cite This: *ACS Appl. Nano Mater.* 2021, 4, 3750–3759 Read Online

ACCESS | Metrics & More | Article Recommendations | Supporting Information

ABSTRACT: The influence of nanoparticle surface facets on electrochromic properties remains largely unexplored in nanostructured "smart" materials. Here, we explore how surface facets influence the coloration efficiency (CE) and long-term optical density (OD) stability of hexagonal WO_3 nanorod (h-WO_3NR) thin films. We synthesized two h-WO_3NR samples with distinct surface facet orientations and studied how the electrochemical, electrochromic, electrical, and surface chemistry properties change after long-term cycling. The sample with unique {$\bar{1}$20} facets exhibited reversible optical switching after 500 cycles and negligible variation in interfacial charge transfer resistance. The ($\bar{1}$20) surface features an open network of square window channels that may enable reversible ion transport and reduced ion trapping, enhancing the optical switching stability. However, the {$\bar{1}$20}-dominant sample exhibited lower CE than the {100}-dominant sample. The reduced optical density changes in the {$\bar{1}$20}-dominant sample could be due to a greater fraction of optically inactive trigonal cavity sites on the {001} end-caps. The results indicate surface facet and particle morphology engineering are viable strategies to enhance the CE and long-term stability/lifetime in electrochromic thin films for smart window applications.

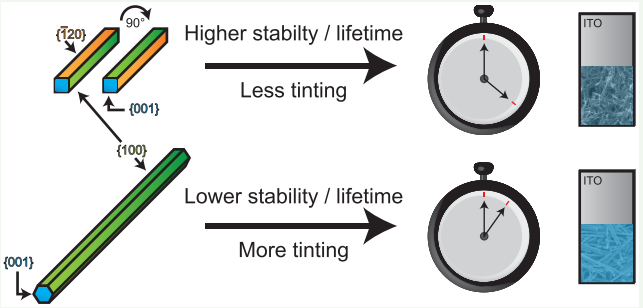

KEYWORDS: *smart windows, electrochromic, crystal facet, hexagonal, tungsten oxide, coloration efficiency, stability*

INTRODUCTION

Electrochromic materials are key components in energy saving smart windows,[1] sensors,[2] self-dimming rear view mirrors,[3] and nonemissive displays.[4] Tungsten oxide is the most widely used inorganic electrochromic material because it is more durable and requires less energy than other metal oxides.[5] h-WO_3 is an attractive ion insertion host relative to triclinic[6] and monoclinic[7] crystalline polymorphs because its large hexagonal channels lead to improved charge storage[8−10] and electrochromic behavior.[11−15] Achieving long-term electrochromic stability (e.g., 30 years lifetime), or the ability to reversibly switch between tinted and transparent states, remains a challenge.[5,16]

Achieving long-term optical modulation stability requires reversible ion insertion/extraction into/out of the WO_3 bulk and across the solid/electrolyte interface. The ion insertion reaction that leads to electrochromic behavior of WO_3 in Li^+-containing electrolytes is given in eq 1 below:

$$WO_3 + xLi^+ + xe^- \rightleftarrows Li_xWO_3 \quad (1)$$

Cathodic polarization of WO_3 induces a double injection of electrons and Li ions, forming a blue Li_xWO_3 compound that strongly absorbs IR radiation.[17] This electrochromic reaction is reversible under anodic conditions, forming the transparent WO_3 compound.

There are several processes that lead to long-term optical degradation of tungsten oxide. Ion trapping, or the trapping of Li ions in the host structure after anodic polarization, is thought to be a major source of optical degradation that reduces the lifetime of electrochromic devices.[18] Doping WO_3 with different combinations of transition metals such as Ti,[19] Nb,[20] and Mo,[21] or introducing oxygen vacancies[22] has been shown to stabilize the crystal structure during ion insertion[19,20] and favorably tune the electronic structure of the material by improving electronic conductivity[22] or ion diffusivity,[21] perhaps circumventing the ion trapping issue.

Surface reactions, such as those involved in solid electrolyte interphase (SEI) layer formation,[23] can also contribute to optical degradation. The SEI layer forms from electrolyte decomposition and can "pinch off" ion insertion.[24−27] Heo et

Received: January 22, 2021
Accepted: March 25, 2021
Published: April 7, 2021

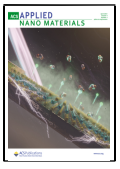

https://doi.org/10.1021/acsanm.1c00215
ACS Appl. Nano Mater. 2021, 4, 3750–3759

al. showed that electrolyte decomposition caused optical degradation in monoclinic $WO_{2.72}$.[28] In that study, the authors demonstrated enhanced Coulombic efficiency and material lifetime by coating the m-$WO_{2.72}$ particle surfaces with 1 nm Al_2O_3 to reduce electrolyte decomposition. Because the surface facet determines the arrangement of atoms exposed to the electrolyte that could participate in SEI formation, we hypothesized that surface facets would influence electrochromic stability.

Facet-dependent electrochromism has been studied in nickel oxide because the coloration mechanism is thought to occur through redox chemistry at the NiO surface;[29,30] changing the surface facet should directly impact tinting and bleaching. The facet orientation alters ion insertion rates because it determines the activation energy for ion diffusion across the interface, which could differ from the bulk.[31] However, surface-facet-dependent electrochromic properties of WO_3 nanoparticles are lacking. In a h-WO_3 battery that also relies on Li-ion insertion, Lian et al. observed that h-WO_3 nanoribbons with an exposed $(\bar{1}20)$ plane exhibited superior electrochemical stability relative to particles with (100) planes.[32] Our group previously studied electrochromic dynamics of individual h-WO_3 NRs and discovered that long NRs exhibited larger optical modulation changes than short NRs.[33] High-resolution electron microscopy analysis suggested that a surface step edge gradient on the long NRs exposed more {001} facets along the width and $\{\bar{1}20\}$ facets along the length.

Motivated by our single particle-level studies[33,34] and WO_3 battery literature,[24,32,35] here we test the hypothesis that exposing more $\{\bar{1}20\}$ facets will improve electrochromic properties and stability of electrochromic h-WO_3 NR (NR) thin films. h-WO_3 is a good model system for this study because it does not undergo a phase transition[11] or large volume expansion during lithiation,[36] minimizing the possibility that changes in bulk structure could complicate data interpretation. We synthesized two WO_3 NR samples with the same hexagonal crystal structure, but one sample exhibited $\{\bar{1}20\}$ facets. In situ electro-optical measurements showed that h-WO_3 NR samples with $\{\bar{1}20\}$ facets exhibited lower CE, but higher optical modulation stability compared to NR samples with {100} and {001} facets.

RESULTS

Two h-WO_3 NR samples with distinct surface facets were synthesized by hydrothermal growth (Scheme 1). Heating an aqueous solution of 1.0 mM ammonium tungstate to 180 °C, vacuum drying, and annealing at 180 °C produced h-WO_3 NRs with $\{\bar{1}20\}$, {100}, and {001} facets (Scheme 1a) according to electron microscopy analyses discussed below. Alternatively, heating an aqueous solution of 0.15 M sodium tungstate precursor in the presence 0.26 M NaCl produced h-WO_3 NRs with {100} and {001} facets (Scheme 1b). The Supporting Information provides detailed synthetic procedures. We refer to these samples as WO_3-$\{\bar{1}20\}$ and WO_3-{100}, according to the unique or dominant surface facet for each sample.

Figure 1a shows the powder X-ray diffraction (PXRD) pattern for the WO_3-$\{\bar{1}20\}$ and WO_3-{100} samples. The diffraction pattern for WO_3-$\{\bar{1}20\}$ and WO_3-{100} were indexed to hexagonal WO_3 ($P6_3/mcm$, JCPDS 04-007-2322 and $P6/mmm$, JCPDS 00-033-1387, respectively). The PXRD peak heights and widths differ between the two samples, suggesting preferred facet orientation among the particles in each sample. The high intensity (100) and low intensity (002)

Scheme 1. Synthesis and Fabrication of h-WO_3 Electrochromic Thin Films: Synthesis, Thin Film Preparation, and Electro-optical Cartoon of (a) WO_3-$\{\bar{1}20\}$ NR and (b) WO_3-{100} NR Thin Films on ITO Substrates

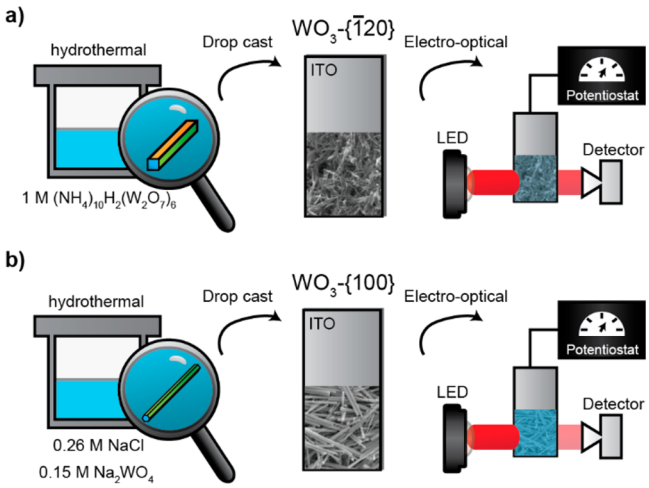

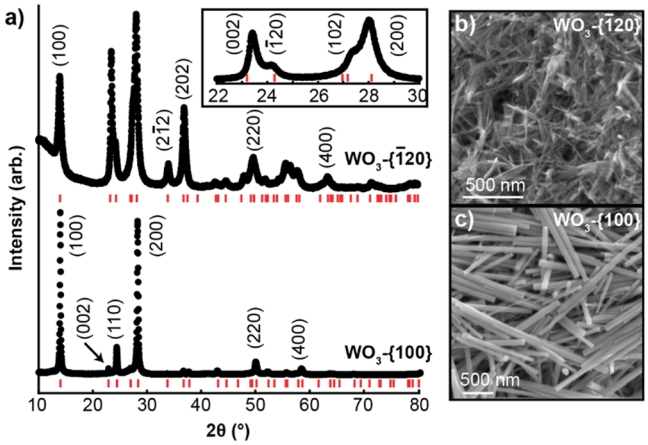

Figure 1. Crystal structure and morphology of h-WO_3NRs. (a) PXRD patterns for WO_3-$\{\bar{1}20\}$ and WO_3-{100} samples (black data points). Red dashes indicate reference peak patterns (top: $P6/mmm$, JCPDS 04-007-2322 WO_3-$\{\bar{1}20\}$; bottom: $P6/mmm$, JCPDS 00-033-1387 WO_3-{100}). (b, c) Representative SEM images of (b) WO_3-$\{\bar{1}20\}$ and (c) WO_3-{100} films.

peak for WO_3-{100} indicate particle growth along the [001] direction with exposed {100} symmetry related planes.[17] However, the PXRD data alone is insufficient to reveal the exposed planes and growth direction of WO_3-$\{\bar{1}20\}$.

Scanning electron microscopy (SEM) images of the WO_3-$\{\bar{1}20\}$ and WO_3-{100} samples exhibit a one-dimensional particle morphology (Figure 1b, c). The median and variance length (l) and width (w) values for the WO_3-$\{\bar{1}20\}$ and WO_3-{100} samples were l = 120 nm ±50 nm and w = 20 nm ±5 nm and l = 980 nm ±480 nm and w = 71 nm ±15 nm, respectively. The smaller WO_3-$\{\bar{1}20\}$ NRs contribute to peak broadening in the PXRD data in Figure 1a. The aspect ratio of both samples were >1 and <20, and therefore, the particles can be categorized as NRs.[37]

The NR growth direction and surface facets were determined using high resolution transmission electron microscopy (HRTEM). Figure 2a, b show HRTEM images for two different NRs from the WO_3-$\{\bar{1}20\}$ sample. Each NR

https://doi.org/10.1021/acsanm.1c00215
ACS Appl. Nano Mater. 2021, 4, 3750−3759

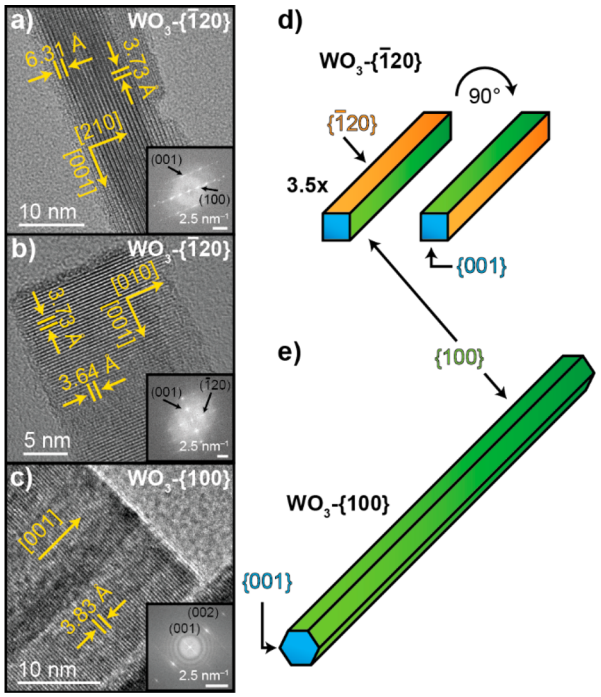

Figure 2. Surface facet characterization and illustration. (a) HRTEM image of a single NR from the WO_3-{1̄20} sample, observed via a top-down view of the {100} surface. (b) HRTEM image of a different single NR in the WO_3-{1̄20} sample, observed via a top-down view of the {1̄20} surface. (c) HRTEM of a single NR in the WO_3-{100} sample. Insets of a–c represent FFT images. (d, e) Cartoon illustration of WO_3-{1̄20} and WO_3-{100} samples drawn to scale (note: 3.5× for WO_3-{1̄20}).

in the film is a single crystal. The lattice spacings in the HRTEM image produce bright spots in the fast Fourier transform (FFT) image (Figure 2a, b inset). The distance between the bright spots in the FFT image correlates to a lattice spacing of 3.73 Å, which can be assigned to planes of atoms along the [001] growth direction. Lattice spacings of 6.31 Å (Figure 2a) or 3.64 Å (Figure 2b) perpendicular to the growth direction each appear roughly half the time and imply rectangular prism geometry; rotating the particle 90° changes the plane of atoms perpendicular to the TEM grid. These spacings, along with the [001] growth direction along the length, indicate that these NR surfaces exhibit {100} and {1̄20} groups of symmetry related planes in the hexagonal system (Figure S1, Table S1). Figure 2c shows a HRTEM image of a single NR in the WO_3-{100} sample. The FFT analysis revealed a lattice spacing of 3.83 Å with no distinct perpendicular spacing, indicating growth along the [001] direction, which is in agreement with literature for WO_3 NRs grown as hexagonal prisms.[17] In summary, these hydrothermal reactions produce 1D hexagonal WO_3 NRs with different length, width, and exposed surface facet orientation.

The cartoon illustrations in Figure 2d, e compare the particle morphology and surface facets of the WO_3-{1̄20} and WO_3-{100} samples. The NRs in the WO_3-{1̄20}sample have a square rectangle morphology. The endcaps are made from {001} planes and the sidewalls are made from {100} and {1̄20} planes. The {1̄20} planes account for 45% of the total NR surface area and the particles likely lay with the long axis parallel to the transparent electrode surface. In this configuration, either the {1̄20} or {100} facet contacts the ITO electrode and the majority of the NR surface area exposed to the electrolyte is from the remaining facets (either {1̄20} or {100}). This configuration is potentially significant for electrochromic thin film electrodes because the facet in contact with the ITO electrode participates in electron transfer whereas those facets in contact with electrolyte undergo interfacial ion insertion processes; the contact resistance and activation energies of these processes could be facet-dependent.[35,38] On the other hand, single NRs in the WO_3-{100} sample exhibit a hexagonal prism morphology, in agreement with literature reports.[17] The sidewalls are composed of symmetrically equivalent (100), (010), and (1̄10) planes (i.e., {100} planes) and the end-caps are composed of {001} planes. These particles also likely lay with the long axis parallel to the ITO electrode. However, the {100} facets are always in contact with the substrate and the electrolyte. Hence, the exposed facets of these two NR samples enables us to study the influence of the {1̄20} facet on electrochromic performance of h-WO_3 NRs.

Having characterized the surface facet orientation of the h-WO_3 NR samples, we prepared WO_3-{1̄20} and WO_3-{100} NR thin films by drop casting 3 mg of sample on ITO substrates. Scanning probe microscopy measurements revealed

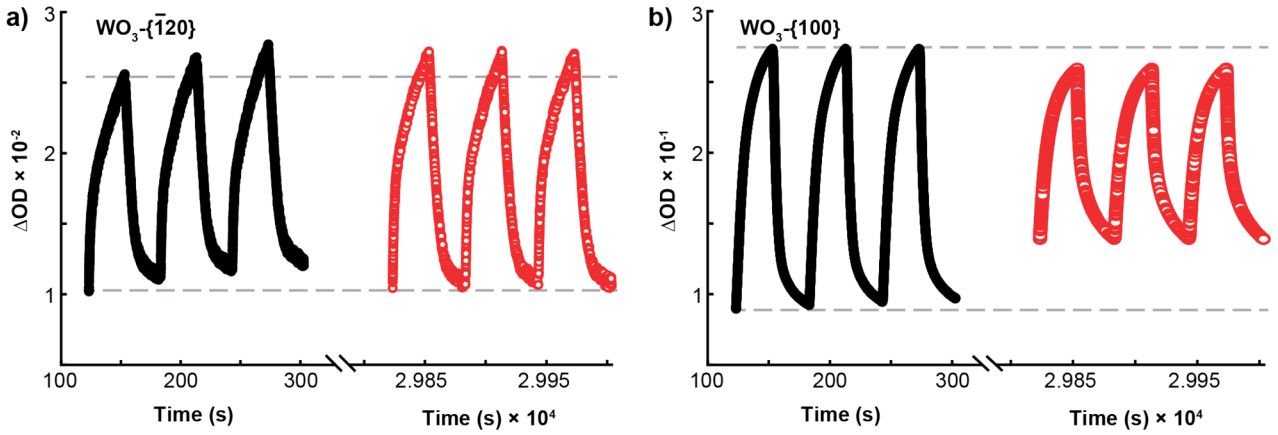

Figure 3. Optical changes at 940 nm. a) ΔOD changes versus time of 474 nm ±170 nm WO_3-{1̄20} films for cycles 3–5 (black filled circles) and 498–500 (red open circles). (b) same as in panel a but for a 1315 nm ± 300 nm WO_3-{100} sample. Horizontal gray lines represent maximum and minimum ΔOD values in cycle 3 and serve as a visual guide for differences between ΔOD in early versus late cycles.

https://doi.org/10.1021/acsanm.1c00215
ACS Appl. Nano Mater. 2021, 4, 3750–3759

the film thicknesses were 474 ± 170 nm and 1315 ± 300 nm for WO_3-{$\bar{1}$20} and WO_3-{100}, respectively (Figure S2). We were unable to prepare uniform h-WO_3 NR thin films of equal thickness on ITO substrates, likely due to the different wettability of the NRs on the ITO surface. Figure 1b, c shows representative SEM images of the film morphology, where the 1D NRs lie with their long axes parallel to the ITO substrate.

Next, we evaluated the electrochromic and electrochemical properties of the thin film electrodes. To do so, we measured the optical density (OD) at 940 nm while cycling the films between −1.0 V for 30 s and 0.5 V for 30 s in 1 M $LiClO_4$/propylenecarbonate (all potential values refer to the Ag/AgCl reference electrode). Figure S3 shows transmission spectra before and after cycling. We measured the intensities of the light transmitted through the h-WO_3 film (I) and a blank ITO reference slide (I_o) and calculated $\mathrm{OD} = -\log_{10}\left(\frac{I}{I_o}\right)$.

To compare the OD magnitude of the films, we calculated the change in optical density, ΔOD, as a function of polarization time according to eq 2:

$$\Delta\mathrm{OD}(t) = \mathrm{OD}(t) - \mathrm{OD}(0) \quad (2)$$

where OD(t) is the OD as a function of cathodic or anodic polarization time and OD(0) is defined as the OD magnitude 100 ms before the potential step is applied at t = 0 s. ΔOD(t) corrects for light absorption and scattering by each film at t = 0 s. Figure 3a, b shows the ΔOD(t) behavior for WO_3-{$\bar{1}$20} and WO_3-{100} films for cycles 3−5 and 498−500. Initial (de)lithiation of both samples produced irreversible electrochromic behavior (cycle 1−2 shown in Figure S4) that could be attributed to ion trapping inside the WO_3 bulk, as discussed and quantified below.[18,39,40] The initial electrochromic response was not surface facet-dependent and, therefore, cycle 1−2 data was omitted from Figure 3a, b to emphasize the electrochromic behavior after repetitive, long-term cycling.

The h-WO_3 samples exhibit different OD magnitudes and cycling behaviors. The ΔOD magnitude of the WO_3-{$\bar{1}$20} sample is an order of magnitude lower than the WO_3-{100} sample. One factor that contributes to the large ΔOD magnitude difference is film thickness. The ΔOD magnitude differs by a factor of 3.0−4.5 after correcting for film thickness (Figure S5). The time required to reach 90% of maximum ΔOD during the cathodic coloration pulse (t_{90}^{bleach}) is ∼20 s for both films and the time required to decay by 90% from maximum ΔOD during the anodic bleach pulse (t_{90}^{bleach}) is ∼15 s for both films (Table S2). Hence, these surface facets do not appear to play a different role in ΔOD kinetics. The tinting behavior of the WO_3-{$\bar{1}$20} sample does not change after the initial cycle. On the other hand, the maximum ΔOD achieved by the WO_3-{100} sample during the tinting pulse decreases by 5% after 500 cycles. Then, upon delithiation, the WO_3-{100} sample does not return to the same transparent state (see gray dashed lines in Figure 3a, b). Specifically, the minimum OD achieved during the bleaching pulse increases by 30% after the initial cycle. The irreversible behavior of WO_3-{100} during the bleaching process suggests that more [Li−W^{5+}] color centers remain trapped in the material after anodic polarization cycles.

To quantify the ion trapping in both films, we calculated the difference between the charge inserted during the cathodic coloration pulse and the charge extracted during the anodic bleaching pulse for cycle 3. The difference in charge was −9.63 × 10^{-3} C and −2.71× 10^{-2} C for WO_3-{$\bar{1}$20} and WO_3-{100}, respectively. The negative sign indicates more charge was inserted in the films during the cathodic pulse than extracted during the anodic pulse. If we assume that 1 Li-ion inserts in the film per injected electron, then the mole fractions of trapped Li ions in the films are 0.0015 and 0.0028 for WO_3-{$\bar{1}$20} and WO_3-{100}, respectively. Ion trapping is more significant in the WO_3-{100} sample.

To explore the origin of the ΔOD magnitude difference between the two samples, we calculated the coloration efficiency (CE) according to eq 3:

$$\mathrm{CE} = \Delta\mathrm{OD}/Q \quad (3)$$

where Q is the total charge density passed as a function of cathodic polarization time (in units of C/cm^2; the area is the geometric area of the film). A large, positive CE value indicates a large optical modulation at 940 nm per number of electrons inserted into the oxide.[41] We determined CE for each cathodic polarization cycle by fitting ΔOD versus Q with a linear function (Figure S6). Figure 4a, b shows CE versus cycle number for the first 30 cycles of each NR film. The CE values of the WO_3-{$\bar{1}$20} and WO_3-{100} films during the first cycle were 24 cm^2 C^{-1} and 25 cm^2 C^{-1}, respectively. Upon cycling, the CE of the WO_3-{100} sample increases steadily with cycle number and plateaus at 80 cm^2 C^{-1} after 45 cycles (Figure 4c). This trend indicates that a significant fraction of charge inserted in WO_3-{100} does not contribute to OD modulation at early cycles. The CE of the WO_3-{$\bar{1}$20} sample increases slowly with cycle number and the relative ΔOD change (optical modulation relative to the first cycle) stays constant after the first cycle. After 500 cycles, the CE value of the WO_3-{100} sample increased by a factor of 233%, whereas the CE value of the WO_3-{$\bar{1}$20} sample only increased by 40%. The large CE increase of the WO_3-{100} film is accompanied by a continuous decrease in ΔOD (Figure 4b). Hence, after 500 cycles, the efficiency of optical modulation increased but the film tinted less. The CE of these NR films differ by a factor of 3, but are within the range reported by Besnardiere et al. for h-

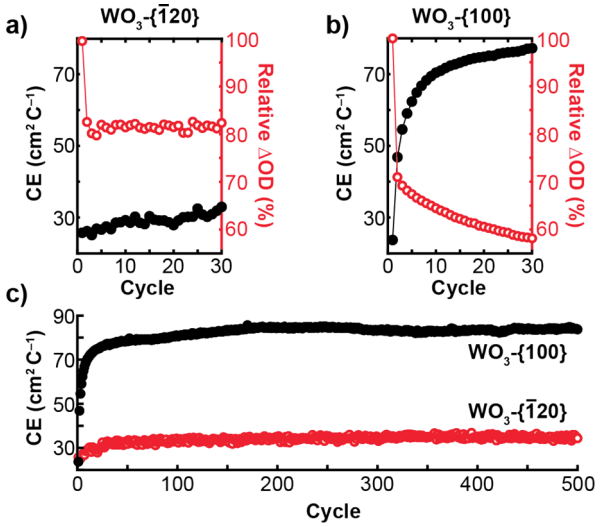

Figure 4. Coloration efficiency of NR samples. (a, b) CE (black filled circles) and relative change in ΔOD (open red circles) for WO_3-{$\bar{1}$20} and WO_3-{100} for the first 30 cycles. Solid lines are a guide for the eye. (c) CE versus cycle number for WO_3-{$\bar{1}$20} and WO_3-{100} films.

https://doi.org/10.1021/acsanm.1c00215
ACS Appl. Nano Mater. 2021, 4, 3750−3759

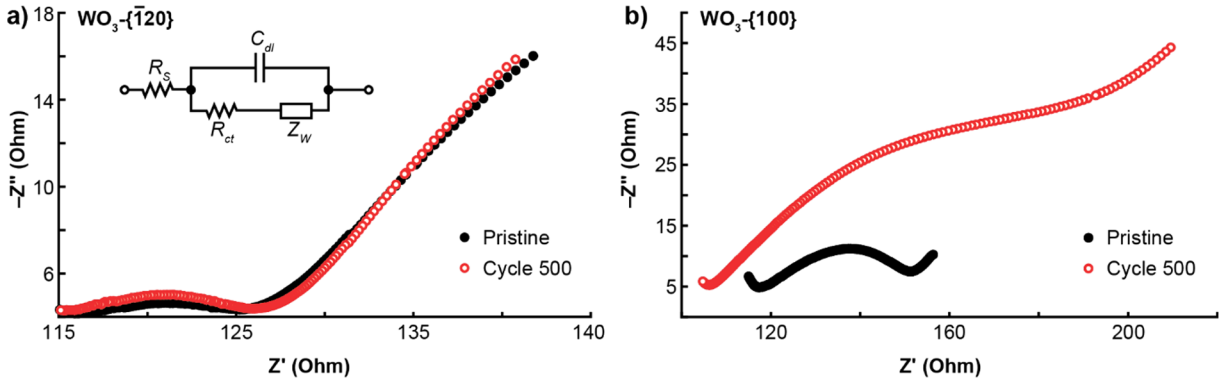

Figure 5. Electrochemical impedance spectroscopy. (a, b) Nyquist plot for the WO_3-{$\bar{1}$20} and WO_3-{100} samples before and after 500 cycles. Data acquired at −1.0 V vs Ag/AgCl over the range of 20 Hz to 150 kHz. The inset in panel a shows the Randle circuit used for fitting EIS data.

WO_3 nanoparticle films (11 cm^2 C^{-1}) and Kondalkar et al. for a conformal nanostructured h-WO_3 film (87.23 cm^2 C^{-1}).[42,43]

To further understand how the surface facets influence electrochromic properties during long-term cycling, we characterized the electrical characteristics of the NR film electrodes before and after cycling using electrochemical impedance spectroscopy (EIS). Figure 5a, b shows Nyquist plots for WO_3-{$\bar{1}$20} and WO_3-{100}, respectively, before and after cycling. Both samples show a semicircle at high frequencies and a linear response at low frequencies. Interestingly, these features did not change after 500 cycles for WO_3-{$\bar{1}$20} (Figure 5a). In contrast, the WO_3-{100} EIS data exhibits significant changes after 500 cycles (Figure 5b). The data shows a larger semicircle over the 1700 to 85 Hz frequency range and a shallower slope at low frequencies after 500 cycles, implying larger charge transfer resistance (R_{ct}) and ionic diffusivity. To quantify the changes in EIS data before and after cycling, we fit the Nyquist plots with the Randle's circuit (Figure 5a inset), which has been used to fit EIS data of electrochromic nanoparticle films,[28,43,44] yielding R_{ct} and the Warburg diffusion element (Z_w). We note that this equivalent circuit assumes semi-infinite diffusion and a planar electrode surface. Because the circuit likely oversimplifies these systems, we focus on the relative trends in fitting parameters for the NR films instead of focusing on absolute values.

Table 1 shows that R_{ct} of the WO_3-{100} sample is initially three times larger than the WO_3-{$\bar{1}$20} sample. The larger R_{ct} could be due to differences in packing density, film thickness, and porosity of the larger NRs. The R_{ct} of the WO_3-{$\bar{1}$20} sample does not change after 500 cycles, whereas R_{ct} of the WO_3-{100} sample doubles after 500 cycles. In addition, Z_w of the WO_3-{100} quadruples after 500 cycles. The changes in fitting parameters indicate that the WO_3-{100} electrode conducts both electrons and Li ions less effectively after 500 cycles.

Table 1. Summary of EIS Fit Result Using a Randle's Circuit to Fit EIS data in Figure 5[a]

	R_{ct} pristine (Ω)	R_{ct} cycle 500 (Ω)	Z_w pristine (Ω)	Z_w cycle 500 (Ω)
WO_3-{$\bar{1}$20}	7.7 ± 0.01	8.8 ± 0.01	23.0 ± 0.01	22.0 ± 0.01
WO_3-{100}	22. ± 0.3	49. ± 0.9	15. ± 0.4	65. ± 1

[a] Z_w was calculated from the fit Warburg constant at 23 Hz.

To understand the origin of the optical and electrical properties of the WO_3-{$\bar{1}$20} and WO_3-{100} electrodes before and after cycling, we examined the surface chemical composition of pristine and cycled films using X-ray photoelectron spectroscopy (XPS) and time-of-flight secondary-ion mass spectroscopy (TOF-SIMS). Figure 6 compares carbon, lithium, oxygen, and tungsten XPS data for pristine and cycled WO_3-{$\bar{1}$20} and WO_3-{100} films; all data normalized to the W $4f_{7/2}$ peak. The trends in XPS data before and after cycling were qualitatively similar for both samples. Below we discuss the changes in XPS data before and after cycling the WO_3-{$\bar{1}$20} film in 1 M $LiClO_4$ in propylene carbonate solvent as a representative example of the surface chemical changes that occur in both h-WO_3 NR film electrodes.

The pristine WO_3-{$\bar{1}$20} film exhibits intense W $4f_{7/2}$ and $4f_{5/2}$ peaks at 35.4 and 37.6 eV, respectively, due to W^{6+}. A prominent oxygen peak at 530.2 eV can be attributed to W−O bonds found in oxides.[45] A small adventitious carbon peak appears at 284.8 eV. After cycling, substantial changes occur in the carbon, lithium, oxygen, and tungsten XPS data. The C 1s data of the WO_3-{$\bar{1}$20} film shows an increase in the adventitious carbon peak at 284.8 eV as well as new peaks at 286.7 and 290.0 eV (Figure 6a). The new peaks can be attributed to C−O and C═O bonds from the carbonate species, respectively, likely due to SEI layer formation as a result of propylene carbonate solvent decomposition.[46] Prominent lithium and oxygen peaks appear at 55.4 eV and 531.7 eV, respectively (Figure 6b, c), further suggesting the presence of lithium carbonate species in the SEI at NR surfaces.[46] However, we were unable to quantify the SEI composition because deconvolution of the O and C 1s signals from propylene carbonate and WO_3 is challenging for these nanostructured films.[47] Nonetheless, the Li XPS data indicates Li ions are a component of the SEI layer. Because the cycling experiments ended on an anodic polarization pulse, we would have expected to observe very little W^{5+} signals in XPS data. However, a W^{5+} shoulder at 34.2 eV is evident in XPS data after 500 cycles (Figure 6d). Therefore, Li ions are likely also trapped at reduced W sites in the NR interior. The relative amount of residual W^{5+} after cycling is 14.6% for WO_3-{$\bar{1}$20} and 20.0% for WO_3-{100}, as determined by peak area comparison. We note a shift in the W and O binding energy after cycling, which could be due to surface charging during the XPS experiment as a result of excess insulating SEI on the {100} facets. TOF-SIMS mapping experiments show qualitatively similar distributions of C, Li, and Cl across the

https://doi.org/10.1021/acsanm.1c00215
ACS Appl. Nano Mater. 2021, 4, 3750−3759

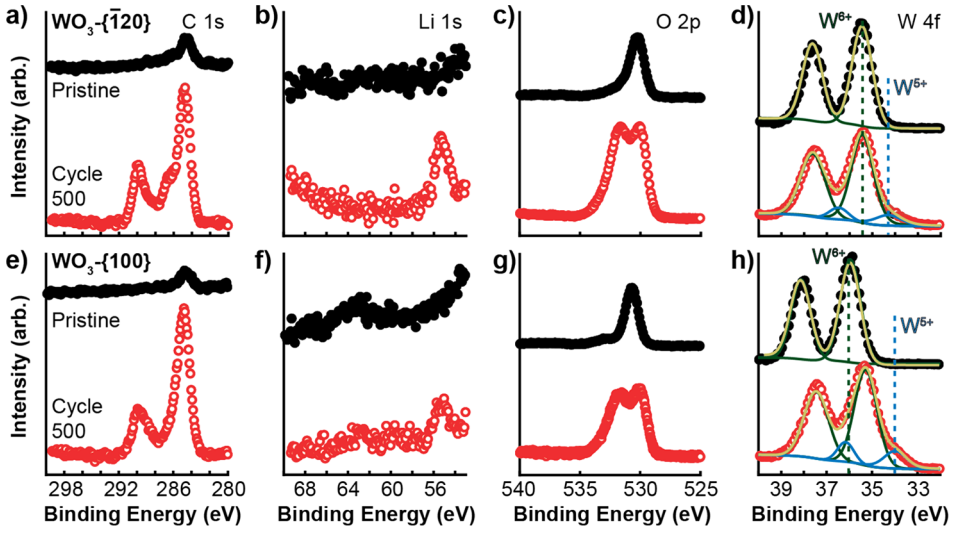

Figure 6. XPS analysis. (a–h) XPS data before (black, filled) and after 500 cycles (red, open) for C 1s, Li 1s, O 2p, and W 4f regions for WO_3-{1̄20} and WO_3-{100} films. W 4f data (d, h) were fit to W $4f_{7/2}$ and $4f_{5/2}$ peaks at 35.4 and 37.6 eV (green), corresponding to W^{6+}. W $4f_{7/2}$ and $4f_{5/2}$ peaks at (d) 34.0 and 36.1 eV and (h) 34.3 and 36.5 eV (blue) were assigned to W^{5+}. The composite fits are shown in gold. All peak intensities are normalized to the tungsten $4f_{7/2}$ peak for each sample.

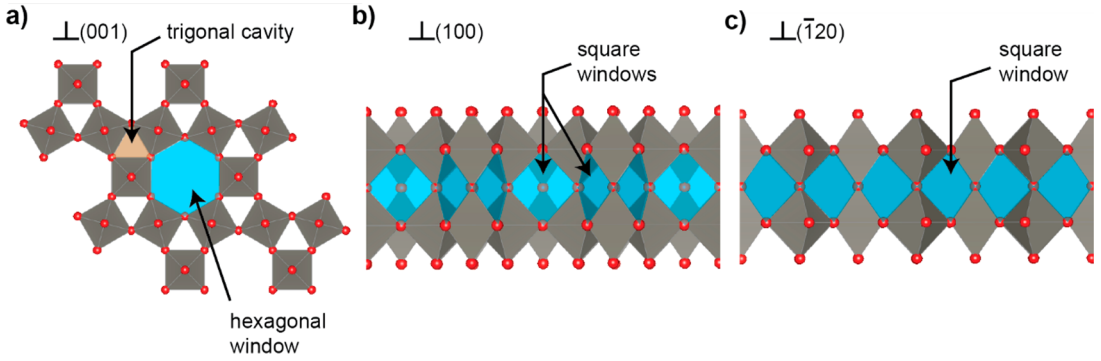

Figure 7. Structure and binding sites in hexagonal WO_3. Top (perpendicular) eye view looking down into the (a) (001) plane showing trigonal cavity and hexagonal window ion binding sites, (b) (100) plane showing square windows, and (c) (1̄20) plane also showing square window sites.

surfaces of both films (Figures S7 and S8). In addition, TOF-SIMS depth profiling measurements revealed similar spatial distribution of Li, W, and C throughout the film thickness, but the carbonaceous layer may be thinner on WO_3-{1̄20} (Figure S9). In summary, XPS and TOF-SIMS data indicate that lithium carbonate-containing SEI layers form on these h-WO_3 samples and the SEI composition does not vary among the samples.

DISCUSSION

On the basis of the literature[32] and our previous single particle-level studies,[33,34] we hypothesized that h-WO_3 particles with dominant {1̄20} facets would exhibit enhanced optical modulation and stability. We observed that {1̄20} facets increased OD stability but decreased CE. Below, we discuss possible explanations for the surface-facet-dependent electrochromic properties.

The WO_3-{100} sample shows two types of optical modulation degradation: coloration degradation (i.e., maximum OD decays in the colored state with increasing cycle number) and transparency degradation (minimum OD decays in the bleached state with increasing cycle number). Both effects have been linked to ion trapping,[39] where Li ions insert in the WO_3 lattice during the coloration step and remain in the host lattice after the bleach step.[18,48,49] The trapping mechanisms and chemical nature of the trapping sites are not entirely understood over a broad range of electrochromic materials.[18,39,40,49−53] These degradation effects are important for electrochromic smart windows because the material is unable to consistently reach a colored or transparent state with increasing on/off cycles. Interestingly, the WO_3-{1̄20}sample does not show either coloration or transparency degradation after the initial cycle (Figure 4a). Instead, coloration and transparency characteristics slightly improve with cycling, though the magnitude of the modulation is always lower for WO_3-{1̄20} than WO_3-{100}.

The lower ΔOD in WO_3-{1̄20} may be explained by a higher fraction of optically inactive sites. Figure 7 shows perpendicular views into the (001), (100), and (1̄20) planes that are present at the surfaces of these NRs (see Figure 2). In addition, Figure 7 illustrates the three Li-ion binding sites in h-WO_3: trigonal cavities, hexagonal windows, and square windows. The hexagonal windows and square windows contribute to OD changes whereas the trigonal cavity site contributes little or no optical activity.[9,12] The trigonal cavity and hexagonal window sites are most easily accessed by the (001) plane (Figure 7a) present on the end-caps of both samples (Figure 2d,e). The WO_3-{1̄20} sample has a larger

https://doi.org/10.1021/acsanm.1c00215
ACS Appl. Nano Mater. 2021, 4, 3750−3759

surface area of {001} planes than the WO_3-{100} sample (8% vs 3% with the geometry illustrated in Figure 2) and, therefore, has more optically inactive trigonal cavity sites at the NR surface. Hence, the lower ΔOD of WO_3-{$\bar{1}$20} NRs may be explained by the fact that Li ions prefer to occupy these optically inactive trigonal cavities[9,12] and those sites are more abundant on WO_3-{$\bar{1}$20} NR surfaces.

The CE increase of the WO_3-{100} film can be attributed to the SEI layer formation process. In this scenario, applying cathodic polarization to the pristine materials induces an interfacial charge transfer reaction where solvent molecules are reduced at the NR surfaces. This SEI layer formation process reduces CE because injected electrons reduce solvent molecules instead of contributing to an OD increase at 940 nm. SEI growth diminishes with increasing cycle number presumably because the insulating surface coating inhibits the electro-reduction reaction.[54] This SEI formation process consumes more charge during initial cycling of the WO_3-{100} sample than the WO_3-{$\bar{1}$20} sample.

The WO_3-{100} sample likely exhibits poor electrochromic stability due to a crowded path for Li ions via (100) planes. Figure 7b, c shows Li-ion insertion pathways via square window sites at the (100) versus ($\bar{1}$20) surfaces. These planes make up the majority of the NR surfaces in the WO_3-{$\bar{1}$20} sample. We speculate that the energy barriers for Li-ion insertion via the different surface planes are not equal due to the different orientation of square window sites. The (100) plane features parallel and perpendicular repeating patterns of square window sites (Figure 7b). This crowded environment differs from the square windows at the ($\bar{1}$20) plane (Figure 7c). We hypothesize the crowded square windows on the (100) plane increase energy barriers for Li-ion insertion, creating Li-ion trapping sites. In this scenario, the overpotential for Li-ion extraction increases as more Li ions occupy crowded square window sites. This effect could explain the long term optical degradation of the colored state in WO_3-{100} NRs. The trapping effect may prevent new Li ions from inserting into the host, which also explains the transparent state degradation in WO_3-{100}.

Another explanation for optical degradation of the WO_3-{100} sample could be growth of an insulating SEI on {100} and {001} planes that induces an overpotential for ion insertion/extraction. EIS data showed a significant increase in R_{ct} in the WO_3-{100} samples that could be attributed to an insulating SEI layer on the {100} planes that account for 95% (area) of WO_3-{100} NR surface area. Depth profiling via TOF-SIMS suggests the SEI layer may be thicker in the WO_3-{100} films (Figure S9). In this scenario, the SEI layer rapidly grows on the {100} planes, contributing to the low CE at early cycle numbers (Figure 4). Ion insertion becomes more difficult with increasing cycle number; increasing cathodic polarization would be required to achieve the same total charge as the early cycle numbers. Ion extraction also becomes more difficult because increasing anodic polarization would be required to depopulate Li ions from stable, low-energy binding sites. This would be unexpected because {$\bar{1}$20} have a higher surface potential than both {100} and {001},[55] and the type/rate of electrolyte decomposition is directly related to the surface potential.[56] However, the XPS and TOF-SIMS data showed no clear facet-dependent SEI characteristics and the mechanism of SEI formation on the different facets of h-WO_3 is not well understood.[57] An alternative hypothesis is that the high-energy {$\bar{1}$20} facet reconstructs under electrochemical conditions. An SEI layer with favorable charge/ion transfer characteristics could form on the reconstructed surface. Surface reconstruction can impact interfacial ion (de)insertion kinetics and also influence disorder in the bulk.[58] In this scenario, the {$\bar{1}$20} surface reconstructs into the lowest available surface potential and influences the location, morphology, or relative abundance of the SEI. In situ TEM or X-ray probe techniques may be necessary to test this hypothesis.

Particle size and shape have been shown to impact OD switching speeds and magnitude in electrochromic WO_3 systems,[59−61] but systematic studies on the role of particle size and shape on coloration or transparency degradation are lacking. One study by Yuan et al. suggested that particle size has little influence on the stability of tetragonal tungsten oxide.[59] There are conflicting reports in the literature on the role of particle size on OD magnitude. Yuan et al. showed increasing particle size increases OD magnitude in tetragonal tungsten oxide films of equivalent thickness,[59] but Kim et al. and Subrahmanyam et al. observed the opposite effect for monoclinic[62] and amorphous[63] systems, respectively. Although it is possible that the particle size could influence extinction spectra via confinement,[13] our large h-WO_3 NRs are not in the confinement regime. The porosity and packing density within the film could influence electrochromic properties,[64,65] but crystallinity was shown to be more impactful.[64] We conclude that particle size differences between these two samples is likely not the dominant contributor to enhanced OD stability in WO_3-{$\bar{1}$20}, but this possibility cannot be excluded.

Mechanical degradation (e.g., cracking, delaminating) of films are known to decrease lifetime of electrochromic devices.[66] SEM imaging before and after electrochemical cycling did not reveal mechanical degradation for WO_3-{100} (Figure S10). h-WO_3 exhibits minimum volume expansion (and no crystalline phase change) during ion insertion,[36] unlike amorphous,[67] triclinic,[6] and monoclinic[7] WO_3 polymorphs. Hence, differences in mechanical degradation likely cannot explain the electrochromic stability enhancement effect.

This facet-dependent study has implications for electrochromic smart windows based on nanoscale materials. The stability enhancement observed for WO_3-{$\bar{1}$20} make it a better choice for electrochromic smart windows compared to WO_3-{100}. A device that can maintain constant optical changes over many cycles is more desirable than one that shows significant degradation after the first 100 cycles. The major benefits for the WO_3-{100} film are the larger OD modulation and increased coloration efficiency. However, thicker WO_3-{$\bar{1}$20} NR films and device optimization may mitigate these shortcomings. In summary, h-WO_3 particles with dominant {$\bar{1}$20} facets could improve the performance of electrochromic smart windows.

CONCLUSION

We synthesized h-WO_3 NR samples with distinct surface facet orientations. The h-WO_3 NR sample with {$\bar{1}$20} facets exhibited more stable long-term electrochromic behavior than NR samples with {001} and {100} surface facets only. The WO_3-{100} film exhibited greater coloration efficiency but diminished total optical modulation after 500 cycles. The type and arrangement of Li-ion binding sites present at the different surface facets likely influence ion trapping and electrochromic reversibility. Our findings suggest that nanoparticle surface facets can be used to optimize the performance of nano-

https://doi.org/10.1021/acsanm.1c00215
ACS Appl. Nano Mater. 2021, 4, 3750−3759

structured electrochromic thin films for smart window applications.

■ ASSOCIATED CONTENT

Supporting Information

The Supporting Information is available free of charge at https://pubs.acs.org/doi/10.1021/acsanm.1c00215.

Experimental methods, structural characterization, and TOF-SIMS characterization (PDF)

■ AUTHOR INFORMATION

Corresponding Author

Justin B. Sambur − *Department of Chemistry and School of Advanced Materials Discovery, Colorado State University, Fort Collins, Colorado 80523, United States;* orcid.org/0000-0002-8457-4946; Email: Justin.Sambur@colostate.edu

Authors

R. Colby Evans − *Department of Chemistry, Colorado State University, Fort Collins, Colorado 80523, United States;* orcid.org/0000-0002-2134-238X

Rachelle Austin − *Department of Chemistry, Colorado State University, Fort Collins, Colorado 80523, United States*

Rebecca C. Miller − *Department of the Vice President for Research, Colorado State University, Fort Collins, Colorado 80523, United States*

Alexander Preston − *School of Advanced Materials Discovery, Colorado State University, Fort Collins, Colorado 80523, United States*

Zach N. Nilsson − *Department of Chemistry, Colorado State University, Fort Collins, Colorado 80523, United States;* orcid.org/0000-0002-2003-2232

Kaka Ma − *School of Advanced Materials Discovery and Department of Mechanical Engineering, Colorado State University, Fort Collins, Colorado 80523, United States;* orcid.org/0000-0002-7763-3389

Complete contact information is available at: https://pubs.acs.org/10.1021/acsanm.1c00215

Author Contributions

R.C.E. performed experiments, analyzed data, and wrote the manuscript. R.A. synthesized materials and performed experiments. R.C.M. analyzed TEM data and provided valuable insight into the facet assignments. Z.N.N. performed SEM and TEM imaging experiments. A.P. performed SPM experiments. A.P. and K.M. analyzed SPM data. J.B.S. and R.C.E. developed the experimental setup, analyzed data, and wrote the manuscript. All authors have given approval to the final version of the manuscript.

Funding

This work was support by the National Science Foundation (DMR- 2046948). This material makes use of the TOF-SIMS system at the Colorado School of Mines, which was supported by the National Science Foundation under Grant 1726898.

Notes

The authors declare no competing financial interest.

■ ACKNOWLEDGMENTS

We thank Steven Marquez and Dr. Roy Geiss at Colorado State University for assistance with SEM imaging during the COVID-19 pandemic. Thanks to Michael Walker for TOF-SIMS. Special thanks to Nathan Gimble at Colorado State University for XPS consultation.

■ REFERENCES

(1) Granqvist, C. G.; Arvizu, M. A.; Bayrak Pehlivan, I.; Qu, H.-Y.; Wen, R.-T.; Niklasson, G. A. Electrochromic Materials and Devices for Energy Efficiency and Human Comfort in Buildings: A Critical Review. *Electrochim. Acta* **2018**, *259*, 1170−1182.

(2) Aller Pellitero, M.; del Campo, F. J. Electrochromic Sensors: Innovative Devices Enabled by Spectroelectrochemical Methods. *Curr. Opin. Electrochem.* **2019**, *15*, 66−72.

(3) Tonar, W. L.; Forgette, J. A.; Anderson, J. S.; Bechtel, J. H.; Carter, J. W.; Stam, J. S. Electrochromic Rearview Mirror Incorporating a Third Surface Partially Transmissive Reflector. U.S. Patent 6512624 B2, January 28, 2003.

(4) Somani, P. R.; Radhakrishnan, S. Electrochromic Materials and Devices: Present and Future. *Mater. Chem. Phys.* **2003**, *77* (1), 117−133.

(5) Wang, Y.; Runnerstrom, E. L.; Milliron, D. J. Switchable Materials for Smart Windows. *Annu. Rev. Chem. Biomol. Eng.* **2016**, *7* (1), 283−304.

(6) Dang, W.; Wang, W.; Yang, Y.; Wang, Y.; Huang, J.; Fang, X.; Wu, L.; Rong, Z.; Chen, X.; Li, X.; Huang, L.; Tang, X. One-Step Hydrothermal Synthesis of 2D WO3 Nanoplates@ Graphene Nanocomposite with Superior Anode Performance for Lithium Ion Battery. *Electrochim. Acta* **2019**, *313*, 99−108.

(7) He, Y.; Gu, M.; Xiao, H.; Luo, L.; Shao, Y.; Gao, F.; Du, Y.; Mao, S. X.; Wang, C. Atomistic Conversion Reaction Mechanism of WO_3 in Secondary Ion Batteries of Li, Na, and Ca. *Angew. Chem.* **2016**, *128* (21), 6352−6355.

(8) Lokhande, V.; Lokhande, A.; Namkoong, G.; Kim, J. H.; Ji, T. Charge Storage in WO_3 Polymorphs and Their Application as Supercapacitor Electrode Material. *Results Phys.* **2019**, *12*, 2012−2020.

(9) Hibino, M. Electrochemical Lithium Intercalation into a Hexagonal WO_3 Framework and Its Structural Change. *Solid State Ionics* **2000**, *135* (1−4), 61−69.

(10) Slade, R.; West, B.; Hall, G. Chemical and Electrochemical Mixed Alkali Metal Insertion Chemistry of the Hexagonal Tungsten Trioxide Framework. *Solid State Ionics* **1989**, *32*−*33*, 154−161.

(11) Delichere, P.; Falaras, P.; Froment, M.; Hugot-Le Goff, A.; Agius, B. ELECTROCHROMISM IN ANODIC WO 3 FILMS I: PREPARATION AND PHYSICOCHEMICAL PROPERTIES OF FILMS IN THE VIRGIN AND COLOURED STATES. *Thin Solid Films* **1988**, *161*, 35−46.

(12) Balaji, S.; Djaoued, Y.; Albert, A.-S.; Ferguson, R. Z.; Brüning, R. Hexagonal Tungsten Oxide Based Electrochromic Devices: Spectroscopic Evidence for the Li Ion Occupancy of Four-Coordinated Square Windows. *Chem. Mater.* **2009**, *21* (7), 1381−1389.

(13) Runnerstrom, E. L.; Llordés, A.; Lounis, S. D.; Milliron, D. J. Nanostructured Electrochromic Smart Windows: Traditional Materials and NIR-Selective Plasmonic Nanocrystals. *Chem. Commun.* **2014**, *50* (73), 10555−10572.

(14) Wang, J. M.; Sun, X. W.; Jiao, Z. Application of Nanostructures in Electrochromic Materials and Devices: Recent Progress. *Materials* **2010**, *3* (12), 5029−5053.

(15) Li, C.-P.; Wolden, C. A.; Dillon, A. C.; Tenent, R. C. Electrochromic Films Produced by Ultrasonic Spray Deposition of Tungsten Oxide Nanoparticles. *Sol. Energy Mater. Sol. Cells* **2012**, *99*, 50−55.

(16) Wu, W.; Wang, M.; Ma, J.; Cao, Y.; Deng, Y. Electrochromic Metal Oxides: Recent Progress and Prospect. *Adv. Electron. Mater.* **2018**, *4* (8), 1800185.

(17) Wang, J.; Khoo, E.; Lee, P. S.; Ma, J. Synthesis, Assembly, and Electrochromic Properties of Uniform Crystalline WO_3 Nanorods. *J. Phys. Chem. C* **2008**, *112* (37), 14306−14312.

(18) Wen, R.-T.; Granqvist, C. G.; Niklasson, G. A. Eliminating Degradation and Uncovering Ion-Trapping Dynamics in Electrochromic WO_3 Thin Films. *Nat. Mater.* **2015**, *14*, 996.
(19) Arvizu, M. A.; Triana, C. A.; Stefanov, B. I.; Granqvist, C. G.; Niklasson, G. A. Electrochromism in Sputter-Deposited W-Ti Oxide Films: Durability Enhancement Due to Ti. *Sol. Energy Mater. Sol. Cells* **2014**, *125*, 184−189.
(20) Bathe, S. R.; Patil, P. S. Influence of Nb Doping on the Electrochromic Properties of WO_3 Films. *J. Phys. D: Appl. Phys.* **2007**, *40* (23), 7423−7431.
(21) Zhou, D.; Shi, F.; Xie, D.; Wang, D. H.; Xia, X. H.; Wang, X. L.; Gu, C. D.; Tu, J. P. Bi-Functional Mo-Doped WO_3 Nanowire Array Electrochromism-plus Electrochemical Energy Storage. *J. Colloid Interface Sci.* **2016**, *465*, 112−120.
(22) Wang, W.; Janotti, A.; Van de Walle, C. G. Role of Oxygen Vacancies in Crystalline WO_3. *J. Mater. Chem. C* **2016**, *4* (27), 6641−6648.
(23) Peled, E. The Electrochemical Behavior of Alkali and Alkaline Earth Metals in Nonaqueous Battery Systems—The Solid Electrolyte Interphase Model. *J. Electrochem. Soc.* **1979**, *126* (12), 2047.
(24) Liu, R.-R.; Deng, X.; Liu, X.-R.; Yan, H.-J.; Cao, A.-M.; Wang, D. Facet Dependent SEI Formation on the $LiNi_{0.5}Mn_{1.5}O_4$ Cathode Identified by in Situ Single Particle Atomic Force Microscopy. *Chem. Commun.* **2014**, *50* (99), 15756−15759.
(25) Sun, C. H.; Yang, X. H.; Chen, J. S.; Li, Z.; Lou, X. W.; Li, C.; Smith, S. C.; Lu, G. Q.; Yang, H. G. Higher Charge/Discharge Rates of Lithium-Ions across Engineered TiO_2 Surfaces Leads to Enhanced Battery Performance. *Chem. Commun.* **2010**, *46* (33), 6129.
(26) Hirayama, M.; Ido, H.; Kim, K.; Cho, W.; Tamura, K.; Mizuki, J.; Kanno, R. Dynamic Structural Changes at $LiMn_2O_4$ /Electrolyte Interface during Lithium Battery Reaction. *J. Am. Chem. Soc.* **2010**, *132* (43), 15268−15276.
(27) Morgan, B. J.; Carrasco, J.; Teobaldi, G. Variation in Surface Energy and Reduction Drive of a Metal Oxide Lithium-Ion Anode with Stoichiometry: A DFT Study of Lithium Titanate Spinel Surfaces. *J. Mater. Chem. A* **2016**, *4* (43), 17180−17192.
(28) Heo, S.; Dahlman, C. J.; Staller, C. M.; Jiang, T.; Dolocan, A.; Korgel, B. A.; Milliron, D. J. Enhanced Coloration Efficiency of Electrochromic Tungsten Oxide Nanorods by Site Selective Occupation of Sodium Ions. *Nano Lett.* **2020**, *20* (3), 2072−2079.
(29) Wen, R.-T.; Granqvist, C. G.; Niklasson, G. A. Anodic Electrochromism for Energy-Efficient Windows: Cation/Anion-Based Surface Processes and Effects of Crystal Facets in Nickel Oxide Thin Films. *Adv. Funct. Mater.* **2015**, *25* (22), 3359−3370.
(30) Guo, J.; Wang, M.; Dong, G.; Zhang, Z.; Zhang, Q.; Yu, H.; Xiao, Y.; Liu, Q.; Liu, J.; Diao, X. Mechanistic Insights into the Coloration, Evolution, and Degradation of NiO_x Electrochromic Anodes. *Inorg. Chem.* **2018**, *57* (15), 8874−8880.
(31) Benedek, P.; Forslund, O. K.; Nocerino, E.; Yazdani, N.; Matsubara, N.; Sassa, Y.; Jurànyi, F.; Medarde, M.; Telling, M.; Månsson, M.; Wood, V. Quantifying Diffusion through Interfaces of Lithium-Ion Battery Active Materials. *ACS Appl. Mater. Interfaces* **2020**, *12* (14), 16243−16249.
(32) Lian, C.; Xiao, X.; Chen, Z.; Liu, Y.; Zhao, E.; Wang, D.; Chen, C. Preparation of Hexagonal Ultrathin WO_3 Nano-Ribbons and Their Electrochemical Performance as an Anode Material in Lithium Ion Batteries. *Nano Res.* **2016**, *9* (2), 435−441.
(33) Evans, R. C.; Ellingworth, A.; Cashen, C. J.; Weinberger, C. R.; Sambur, J. B. Influence of Single-Nanoparticle Electrochromic Dynamics on the Durability and Speed of Smart Windows. *Proc. Natl. Acad. Sci. U. S. A.* **2019**, *116* (26), 12666−12671.
(34) Evans, R. C.; Nilsson, Z.; Balch, B.; Wang, L.; Neilson, J. R.; Weinberger, C. R.; Sambur, J. B. Quantifying Capacitive-Like and Battery-Like Charge Storage Contributions Using Single-Nanoparticle Electro-Optical Imaging. *ChemElectroChem* **2020**, *7* (3), 753−760.
(35) Hai, B.; Shukla, A. K.; Duncan, H.; Chen, G. The Effect of Particle Surface Facets on the Kinetic Properties of $LiMn_{1.5}Ni_{0.5}O_4$ Cathode Materials. *J. Mater. Chem. A* **2013**, *1* (3), 759−769.
(36) Oi, J.; Kishimoto, A.; Kudo, T.; Hiratani, M. Hexagonal Tungsten Trioxide Obtained from Peroxo-Polytungstate and Reversible Lithium Electro-Intercalation into Its Framework. *J. Solid State Chem.* **1992**, *96* (1), 13−19.
(37) Murphy, C. J.; Jana, N. R. Controlling the Aspect Ratio of Inorganic Nanorods and Nanowires. *Adv. Mater.* **2002**, *14* (1), 80−82.
(38) Wang, Q.; Shen, L.; Xue, T.; Cheng, G.; Huang, C. Z.; Fan, H. J.; Feng, Y. P. Single-Crystalline TiO_2(B) Nanobelts with Unusual Large Exposed 100 Facets and Enhanced Li-Storage Capacity. *Adv. Funct. Mater.* **2021**, *31* (2), 2002187.
(39) Dong, D.; Wang, W.; Rougier, A.; Barnabé, A.; Dong, G.; Zhang, F.; Diao, X. Lithium Trapping as a Degradation Mechanism of the Electrochromic Properties of All-Solid-State WO_3//NiO Devices. *J. Mater. Chem. C* **2018**, *6* (37), 9875−9889.
(40) Bisquert, J. Analysis of the Kinetics of Ion Intercalation - Ion Trapping Approach to Solid-State Relaxation Processes. *Electrochim. Acta* **2002**, *47* (15), 2435−2449.
(41) Granqvist, C. G. Handbook of Inorganic Electrochromic Materials; *Tungsten Oxide Films: Optical Properties In The luminous And Near-Infrared Range.*; Elsevier Science: Amsterdam, 1995; pp 147−173.
(42) Besnardiere, J.; Ma, B.; Torres-Pardo, A.; Wallez, G.; Kabbour, H.; González-Calbet, J. M.; Von Bardeleben, H. J.; Fleury, B.; Buissette, V.; Sanchez, C.; Le Mercier, T.; Cassaignon, S.; Portehault, D. Structure and Electrochromism of Two-Dimensional Octahedral Molecular Sieve h'-WO_3. *Nat. Commun.* **2019**, *10* (1), 327.
(43) Kondalkar, V. V.; Mali, S. S.; Kharade, R. R.; Khot, K. V.; Patil, P. B.; Mane, R. M.; Choudhury, S.; Patil, P. S.; Hong, C. K.; Kim, J. H.; Bhosale, P. N. High Performing Smart Electrochromic Device Based on Honeycomb Nanostructured H-WO_3 Thin Films: Hydrothermal Assisted Synthesis. *Dalton Trans.* **2015**, *44* (6), 2788−2800.
(44) Li, Y.; McMaster, W. A.; Wei, H.; Chen, D.; Caruso, R. A. Enhanced Electrochromic Properties of WO_3 Nanotree-like Structures Synthesized via a Two-Step Solvothermal Process Showing Promise for Electrochromic Window Application. *ACS Appl. Nano Mater.* **2018**, *1* (6), 2552−2558.
(45) Vasilopoulou, M.; Soultati, A.; Georgiadou, D. G.; Stergiopoulos, T.; Palilis, L. C.; Kennou, S.; Stathopoulos, N. A.; Davazoglou, D.; Argitis, P. Hydrogenated Under-Stoichiometric Tungsten Oxide Anode Interlayers for Efficient and Stable Organic Photovoltaics. *J. Mater. Chem. A* **2014**, *2* (6), 1738−1749.
(46) Kanamura, K.; Tamura, H.; Takehara, Z. XPS Analysis of a Lithium Surface Immersed in Propylene Carbonate Solution Containing Various Salts. *J. Electroanal. Chem.* **1992**, *333* (1−2), 127−142.
(47) Stickle, W.; Stickle, T. Propylene Carbonate - XPS Reference Spectra. *Surf. Sci. Spectra* **2014**, *21* (1), 28−34.
(48) Arvizu, M. A.; Wen, R.-T.; Primetzhofer, D.; Klemberg-Sapieha, J. E.; Martinu, L.; Niklasson, G. A.; Granqvist, C. G. Galvanostatic Ion Detrapping Rejuvenates Oxide Thin Films. *ACS Appl. Mater. Interfaces* **2015**, *7* (48), 26387−26390.
(49) Baloukas, B.; Arvizu, M. A.; Wen, R.-T.; Niklasson, G. A.; Granqvist, C. G.; Vernhes, R.; Klemberg-Sapieha, J. E.; Martinu, L. Galvanostatic Rejuvenation of Electrochromic WO_3 Thin Films: Ion Trapping and Detrapping Observed by Optical Measurements and by Time-of-Flight Secondary Ion Mass Spectrometry. *ACS Appl. Mater. Interfaces* **2017**, *9* (20), 16995−17001.
(50) Wen, R.-T.; Arvizu, M. A.; Morales-Luna, M.; Granqvist, C. G.; Niklasson, G. A. Ion Trapping and Detrapping in Amorphous Tungsten Oxide Thin Films Observed by Real-Time Electro-Optical Monitoring. *Chem. Mater.* **2016**, *28* (13), 4670−4676.
(51) Bisquert, J. Fractional Diffusion in the Multiple-Trapping Regime and Revision of the Equivalence with the Continuous-Time Random Walk. *Phys. Rev. Lett.* **2003**, *91* (1), 10602.
(52) Bisquert, J. Beyond the Quasistatic Approximation: Impedance and Capacitance of an Exponential Distribution of Traps. *Phys. Rev. B: Condens. Matter Mater. Phys.* **2008**, *77* (23), 235203.

https://doi.org/10.1021/acsanm.1c00215
ACS Appl. Nano Mater. 2021, 4, 3750−3759

(53) Jiménez, J. M.; Bourret, G. R.; Berger, T.; McKenna, K. P. Modification of Charge Trapping at Particle/Particle Interfaces by Electrochemical Hydrogen Doping of Nanocrystalline TiO_2. *J. Am. Chem. Soc.* **2016**, *138* (49), 15956−15964.
(54) Wang, A.; Kadam, S.; Li, H.; Shi, S.; Qi, Y. Review on Modeling of the Anode Solid Electrolyte Interphase (SEI) for Lithium-Ion Batteries. *Npj Comput. Mater.* **2018**, *4* (1), 1−26.
(55) Wang, X.; Tian, F. H.; Zhao, W.; Fu, A.; Zhao, L. Surface Stabilization of Hexagonal WO_3 by Non-Metallic Atoms: A DFT Study. *Comput. Mater. Sci.* **2013**, *68*, 218−221.
(56) Goodenough, J. B.; Kim, Y. Challenges for Rechargeable Li Batteries. *Chem. Mater.* **2010**, *22* (3), 587−603.
(57) Wang, A.; Kadam, S.; Li, H.; Shi, S.; Qi, Y. Review on Modeling of the Anode Solid Electrolyte Interphase (SEI) for Lithium-Ion Batteries. *Npj Comput. Mater.* **2018**, *4* (1), 15.
(58) Li, S.; Jiang, Z.; Han, J.; Xu, Z.; Wang, C.; Huang, H.; Yu, C.; Lee, S.-J.; Pianetta, P.; Ohldag, H.; Qiu, J.; Lee, J.-S.; Lin, F.; Zhao, K.; Liu, Y. Mutual Modulation between Surface Chemistry and Bulk Microstructure within Secondary Particles of Nickel-Rich Layered Oxides. *Nat. Commun.* **2020**, *11* (1), 4433.
(59) Yuan, G.; Hua, C.; Khan, S.; Jiang, S.; Wu, Z.; Liu, Y.; Wang, J.; Song, C.; Han, G. Improved Electrochromic Performance of WO_3 Films with Size Controlled Nanorods. *Electrochim. Acta* **2018**, *260*, 274−280.
(60) Vemuri, R. S.; Bharathi, K. K.; Gullapalli, S. K.; Ramana, C. V. Effect of Structure and Size on the Electrical Properties of Nanocrystalline WO_3 Films. *ACS Appl. Mater. Interfaces* **2010**, *2* (9), 2623−2628.
(61) Lee, S.-H.; Deshpande, R.; Parilla, P. A.; Jones, K. M.; To, B.; Mahan, A. H.; Dillon, A. C. Crystalline WO_3 Nanoparticles for Highly Improved Electrochromic Applications. *Adv. Mater.* **2006**, *18* (6), 763−766.
(62) Kim, H.; Choi, D.; Kim, K.; Chu, W.; Chun, D.-M.; Lee, C. S. Effect of Particle Size and Amorphous Phase on the Electrochromic Properties of Kinetically Deposited WO_3 Films. *Sol. Energy Mater. Sol. Cells* **2018**, *177*, 44−50.
(63) Subrahmanyam, A.; Karuppasamy, A. Optical and Electrochromic Properties of Oxygen Sputtered Tungsten Oxide (WO_3) Thin Films. *Sol. Energy Mater. Sol. Cells* **2007**, *91* (4), 266−274.
(64) Sallard, S.; Brezesinski, T.; Smarsly, B. M. Electrochromic Stability of WO_3 Thin Films with Nanometer-Scale Periodicity and Varying Degrees of Crystallinity. *J. Phys. Chem. C* **2007**, *111* (19), 7200−7206.
(65) Schlotter, P. High Contrast Electrochromic Tungsten Oxide Layers. *Sol. Energy Mater.* **1987**, *16* (1), 39−46.
(66) Yoo, S. J.; Lim, J. W.; Sung, Y.-E. Improved Electrochromic Devices with an Inorganic Solid Electrolyte Protective Layer. *Sol. Energy Mater. Sol. Cells* **2006**, *90* (4), 477−484.
(67) Arvizu, M. A.; Qu, H.-Y.; Cindemir, U.; Qiu, Z.; Rojas-González, E. A.; Primetzhofer, D.; Granqvist, C. G.; Österlund, L.; Niklasson, G. A. Electrochromic WO_3 Thin Films Attain Unprecedented Durability by Potentiostatic Pretreatment. *J. Mater. Chem. A* **2019**, *7* (6), 2908−2918.

https://doi.org/10.1021/acsanm.1c00215
ACS Appl. Nano Mater. 2021, 4, 3750−3759